"Biotechnological promises of Fe-filled CNTs for cell shepherding and magnetic fluid hyperthermia applications"

Pineux, F. ; Marega, R. ; Stopin, A. ; La Torre, A. ; Garcia, Yann ; Devlin, E. ; Michiels, C. ; Khlobystov, A. ; Bonifazi, D.

Abstract

Fe-filled carbon nanotubes (Fe@CNTs) recently emerged as an effective class of hybrid nanoparticles for biotechnological applications, such as magnetic cell sorting and magnetic fluid hyperthermia. Aiming at studying the effects of both the Fe loading and the magnetocrystalline characteristics in these applications, we describe herein the preparation of Fe@CNTs containing different Fe phases that, upon functionalization with the antibody Cetuximab (Ctxb), allow the targeting of cancer cells. Our experimental findings reveal that an optimal Ctxb/Fe weight ratio of 1.2 is needed for efficient magnetic cell shepherding, whereas enhanced MFH-induced mortality (70 vs. 15%) can be reached with hybrids enriched in the coercive Fe3C phase. These results suggest that a synergistic effect between the Ab loading and the Fe distribution in each nanotube exists, for which the maximum shepherding and hyperthermia effects are observed when higher densities of Fe@CNTs featuring the more coercive pha...

Document type : *Article de périodique (Journal article)*

Nanoscale

PAPER

View Article Online
View Journal | View Issue

Cite this: *Nanoscale*, 2015, **7**, 20474

Biotechnological promises of Fe-filled CNTs for cell shepherding and magnetic fluid hyperthermia applications†

Florent Pineux,[a] Riccardo Marega,[a] Antoine Stopin,[a] Alessandro La Torre,[b] Yann Garcia,[c] Eamonn Devlin,[d] Carine Michiels,[e] Andrei N. Khlobystov[b] and Davide Bonifazi*[a,f]

Received 19th July 2015,
Accepted 31st August 2015

DOI: 10.1039/c5nr04824a

www.rsc.org/nanoscale

Fe-filled carbon nanotubes (Fe@CNTs) recently emerged as an effective class of hybrid nanoparticles for biotechnological applications, such as magnetic cell sorting and magnetic fluid hyperthermia. Aiming at studying the effects of both the Fe loading and the magnetocrystalline characteristics in these applications, we describe herein the preparation of Fe@CNTs containing different Fe phases that, upon functionalization with the antibody Cetuximab (Ctxb), allow the targeting of cancer cells. Our experimental findings reveal that an optimal Ctxb/Fe weight ratio of 1.2 is needed for efficient magnetic cell shepherding, whereas enhanced MFH-induced mortality (70 *vs.* 15%) can be reached with hybrids enriched in the coercive Fe_3C phase. These results suggest that a synergistic effect between the Ab loading and the Fe distribution in each nanotube exists, for which the maximum shepherding and hyperthermia effects are observed when higher densities of Fe@CNTs featuring the more coercive phase are interfaced with the cells.

1. Introduction

Cancer nanotechnology, *i.e.* the use of nanoparticles as versatile tools to diagnose and treat cancer, emerged in the past decade as a complementary approach to the classical cancer theranostics.[1] Scientists have shown that nanostructured materials can represent an effective multifunctional platform for targeting tumour tissues[2,3] and to locally deliver therapeutic or imaging agents.[4] Among the different kinds of nanoparticles, carbon nanotubes (CNTs) have emerged as effective platforms for cancer theranostics both in *in vitro* and *in vivo* studies.[5–16]

From the structural point of view, the interior cavities of CNTs are exceptional frameworks to confine functional, chemical[17–19] and bioactive[20] molecular species. For instance, radioactive salts[21] like $Na^{125}I$ or toxic Gd^{3+}-based contrast agents[22–25] could be safely encapsulated and used *in vivo* as responsive probes for imaging applications. Alternatively, magnetic nanoparticles (MNPs) utilised for magnetic resonance imaging (MRI),[26] magnetic fluid hyperthermia (MFH)[27] or magnetically-driven delivery,[28] have also been confined inside CNTs (MNPs@CNTs).[29] These materials retain their magnetocrystallinity for years,[30] as the confinement procures protection against oxidation reactions[31,32] and consequent transformation into less-performing magnetic phases.[33] For example, CNTs entrapping Ni catalyst residues have been proposed for *in vitro* magnetically-driven DNA delivery in mammalian cells (also known as "CNT spearing").[34] Similarly, low-content Fe-filled CNTs (around 2.5 Fe wt%) were used by Vittorio *et al.* to manipulate, by means of an external field,[35] neuroblastoma cells[36] or mesenchymal stem cells *in vivo*.[37] Additionally, Fe@CNTs non-covalently coated with pluronic F127 have given promising outcomes as dual MRI contrast agents and laser-induced thermo-active therapeutic platforms.[38] In this respect, we recently reported[39] on the functionalisation of Fe@CNTs (prepared *via* the floating-catalyst chemical vapour deposition,

[a]*Department of Chemistry and Namur Research College (NARC), University of Namur, Rue de Bruxelles 61, Namur, 5000, Belgium. E-mail: davide.bonifazi@unamur.be*
[b]*School of Chemistry, University of Nottingham, University Park, Nottingham, NG7 2RD, UK*
[c]*Institute of Condensed Matter and Nanosciences, Molecules, Solids and Reactivity (IMCN/MOST), Université Catholique de Louvain, Place L. Pasteur 1, Louvain-la-Neuve, 1348, Belgium*
[d]*Institute for Advanced Materials, Physicochemical Processes, Nanotechnology and Microsystems, NCSR 'Demokritos', Aghia Paraskevi, 15310 Athens, Greece*
[e]*Unité de Recherche en Biologie Cellulaire (URBC) and NARILIS, University of Namur, Rue de Bruxelles 61, Namur, 5000, Belgium*
[f]*Department of Chemical and Pharmaceutical Sciences and INSTM UdR Trieste, University of Trieste, Piazzale Europa, 34127 Trieste, Italy*
†Electronic supplementary information (ESI) available. See DOI: 10.1039/c5nr04824a

FC-CVD, protocol[40,41] for Fe loading >15 wt%) with cetuximab,[42] an antibody (Ab) targeting the epidermal growth factor receptor (EGFR) overexpressed in cancer cells. *In vitro* investigations under a static magnetic field showed that this material undergoes fast translation responses allowing us to sort EGFR+ cancer cells over a healthy cell population (EGFR−). Furthermore, a notable cytotoxic effect on the cancer cells was observed upon application of an alternating magnetic field (83 kA m^{-1} and 220 kHz). After the primary work by Büchner and coworkers,[43] this has represented the first report about the biotechnological potential of Fe@CNTs as a versatile scaffold for *in vitro* MFH therapy. Exploiting the chemical vapour deposition methodology and post-synthetic treatments (mineral acid[44,45] or thermal[46–48]), in this work we comprehensively describe the preparation and the magnetic-dependent physical properties of Fe-filled CNTs that differ in the Fe content (20 to 35 wt%) and crystalline phase (α-Fe, Fe_3C, γ-Fe_2O_3 and γ-Fe). The structural, morphological and magnetic properties were characterized by X-ray photoelectron spectroscopy (XPS), powder X-ray diffraction (PXRD), ^{57}Fe-Mössbauer (^{57}Fe-MS), transmission electron microscopy (TEM), thermogravimetric analysis (TGA), superconducting quantum interference device (SQUID) and magnetic and thermal measurements (specific absorption rate, SAR). Subsequent bioconjugation with cetuximab led to functional materials for magnetic filtration and MFH therapy applications, whose efficiency resulted to be dependent on both the content and type of the confined Fe phases.

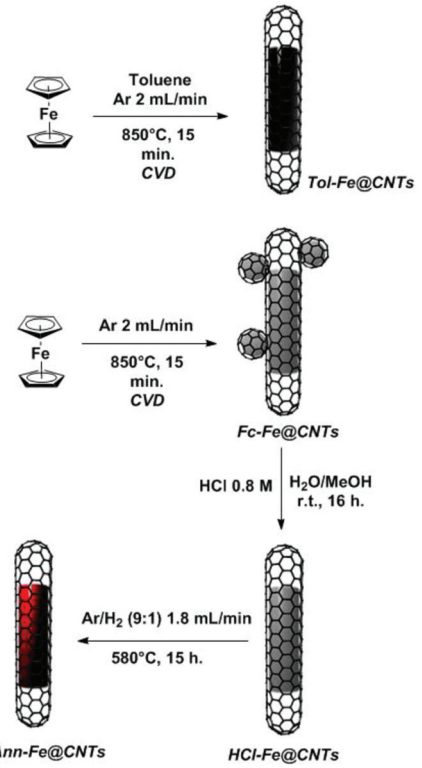

Scheme 1 Synthetic routes for the preparation of magnetic Fe@CNTs.

2. Results and discussion

2.1 Synthesis and physicochemical characterization of Fe@CNTs

The FC-CVD process uses organometallic compounds, such as ferrocene[49] (Fc) or cobaltocene,[50] serving as both metal and carbon atom sources, with or without a complementary carbon feedstock. These organometallic species form metallic nanoparticles at high temperature (>600 °C) that catalyse the growth of MNPs@CNTs. During this process, the MNPs undergo spontaneous encapsulation into graphitic nanoparticles.[51,52] Among the multitude of the FC-CVD methods for growing CNTs,[38,49,50,53–73] significant structural and compositional differences exist in terms of length, diameter, number of walls, MNP loading, chemical composition, crystallinity, and morphology. As a general trend, the FC-CVD technique produces structurally homogeneous Fe@CNTs,[74] displaying limited amounts of Fe (2–10 Fe wt%, with M_s values below 10 emu g^{-1})[43] when complementary carbon feedstock like EtOH, toluene or acetylene is used.[41,63,72,75] On the other hand, protocols employing only Fc lead to structurally-inhomogeneous Fe@CNTs, with higher Fe loadings (up to 50 wt%) and enhanced M_s values (between 40 and 60 emu g^{-1}).[53,59,76] Literature studies showed that the temperature of Fc-sublimation (T_{sub})[53,76] and synthesis (T_{synth})[76] are crucial for controlling the morphology of the material. Too low T_{sub} (<160 °C) leads to the preferential formation of core–shell nanoparticles, in which the Fe phases are wrapped in several graphitic layers (Fe@CNPs).[53]

Based on these literature premises, we prepared Fe@CNT hybrids possessing different Fe contents using the FC-CVD protocol with Fc sublimation either at 350 °C (**Fc-Fe@CNTs**, Scheme 1) or at 550 °C with toluene as a complementary source of carbon (**Tol-Fe@CNTs**). We thus evaluated the amount and quality of the exohedrally- and endohedrally-confined Fe phases through a combination of macroscopic (TGA, XPS, EDX, PXRD and ^{57}Fe-MS analysis) and microscopic (TEM) techniques.

TGA analyses of **Fc-Fe@CNTs** and **Tol-Fe@CNTs** displayed remarkable Fe loadings of about 36 and 24 wt%, respectively (Table 1 and Fig. 1.2a–d). As the XPS investigations only displayed the presence of C and O binding energies, the spectra revealed only minor amounts of Fe (0.8 ± 0.2 at% for **Fc-Fe@CNTs** and 0.3 ± 0.0 at% for **Tol-Fe@CNTs**), thus suggesting that only traces of Fe are present at the exosurface of the nanotubes. While both metallic and oxidised Fe particles are observed for **Fc-Fe@CNTs** (peaks centred at 707 and 712 eV, respectively, Fig. 1.3a–d), only metallic phases are present in **Tol-Fe@CNTs** (Fig. 1.3d). TGA profiles under air (Fig. 1.2a–d) displayed the presence of a 4 wt% increase before the graphitic oxidation event (at about 480 °C) for the samples containing **Fc-Fe@CNTs** (Fig. 1.2a), thus suggesting the formation of Fe oxides most likely derived from non-fully

Table 1 Fe compositional assessment as determined by XPS, ^{57}Fe-MS and TGA under air

Hybrid	XPS (at% ± SD)	TGA under air (wt%)	^{57}Fe-MS (abundance (%))			
			Fe_3C	α-Fe	γ-Fe	γ-Fe_2O_3
Fc-Fe@CNTs	0.8 (±0.2)	35.8	76	10	5	9
HCl-Fe@CNTs	0.2 (±0.0)	19.0	88	5	7	0
Ann-Fe@CNTs	—	22.1	54	44	2	0
Tol-Fe@CNTs	0.3 (±0.0)	23.8	98	0	2	0

encapsulated Fe phases. ^{57}Fe-MS (Fig. 1.1a–d) and PXRD spectra (Fig. S1†) displayed the presence of four Fe phases for **Fc-Fe@CNTs** (Fe_3C, and lower amounts of α-Fe, γ-Fe and γ-Fe_2O_3) and essentially Fe_3C with some traces of γ-Fe for samples containing **Tol-Fe@CNTs** (Fig. 1.1d). Given the recent discoveries about the seeding role of Fe_3C particles in the growth of CNTs,[77] we can reasonably think that Fe_3C NPs are initially formed and subsequently govern the CNT growth. Consequently, the high loading of Fe_3C found in the **Tol-Fe@CNT** samples is most likely derived from the higher C/Fe ratio of the feedstock (*i.e.*, toluene/Fc) during the CVD process compared to the conditions used for **Fc-Fe@CNTs**.

To remove the non-encapsulated Fe, **Fc-Fe@CNTs** were washed several times with an aqueous HCl solution (Scheme 1). This enabled a stepwise reduction of the Fe loading after the first and the second washing cycles, producing **HCl-Fe@CNTs** displaying 19 wt% of Fe as determined by TGA (Fig. 1.2b). Notably, a strong decrease in both α-Fe and γ-Fe_2O_3 phases was observed, leading to samples enriched in Fe_3C as measured by ^{57}Fe-MS (Fig. 1.1b), PXRD (Fig. S1†) and XPS (Fe 2p peak disappearance in the XPS spectrum after washing Fig. 1.3b). These acid-induced changes of both composition and crystallinity of the Fe phases have also been previously reported in the literature.[44] Aiming at increasing the content of the α-Fe phase by thermal disproportionation of

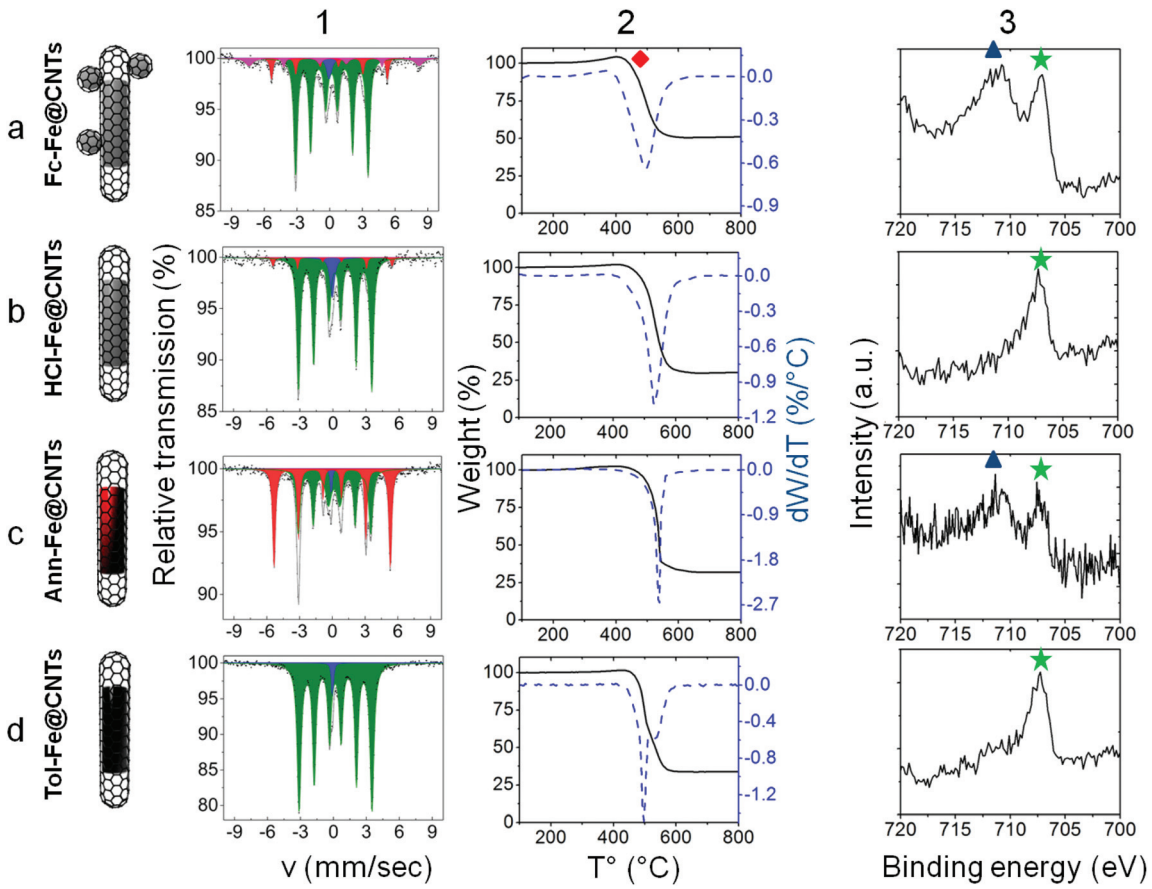

Fig. 1 (1) ^{57}Fe-Mössbauer, (2) TGA under air and (3) Fe 2p XPS profiles for (a) **Fc-Fe@CNTs**, (b) **HCl-Fe@CNTs**, (c) **Ann-Fe@CNTs** and (d) **Tol-Fe@CNTs**. In the ^{57}Fe-Mössbauer spectra (1a–d), the singlet is assigned to paramagnetic γ-Fe (blue colour); the sextet with δ = 0.19(1) mm s^{-1}, quadrupole shift ε = 0.01(1) mm s^{-1} and hyperfine magnetic field (B_{hf}) of 20.6 T corresponds to Fe_3C (green colour); the sextet with zero isomer and quadrupole shifts indicates a cubic symmetry (B_{hf} = 33.1 T), typical for ferromagnetic α-Fe (red colour); the sextet with δ = 0.34(6) mm s^{-1}, ε = 0.05 (6) mm s^{-1} and B_{hf} = 48.3(4) T indicates the presence of traces of γ-Fe_2O_3 (pink colour). Hyperfine parameters are gathered in Table S1.† The TGA profiles are displayed as temperature-modulated weight% (—) and differential weight% (-----) (2a–d). The red square indicates a pronounced weight gain before the pyrolysis event in **Fc-Fe@CNTs**. XPS high-resolution spectra (3a–d) show the presence of oxidised (blue triangles) and metallic (green stars) Fe 2p peaks, both attributed to the most superficial Fe phases.

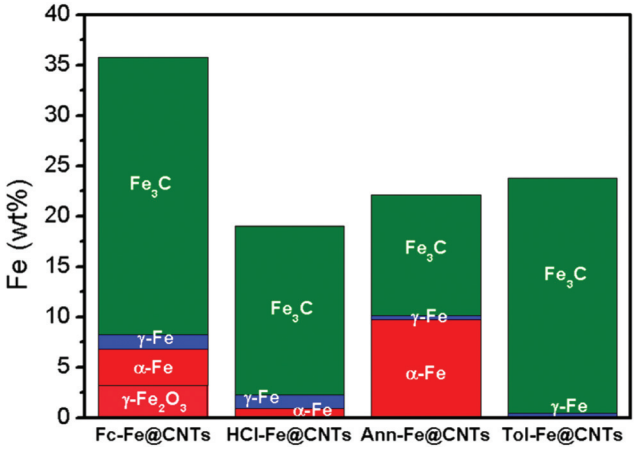

Fig. 2 Histogram distribution of the Fe phases in the four materials as assessed by ^{57}Fe-Mössbauer spectroscopy and TGA measurements under air.

Fe_3C, α-Fe-enriched samples were prepared by adaptation of literature protocols.[47,48] **HCl-Fe@CNTs** were heated at 580 °C under an Ar/H_2 flow for 15 h to afford annealed Fe-filled CNTs, **Ann-Fe@CNTs** (Scheme 1). Notably, the annealing protocol caused a slight increase in the total Fe ratio (from 19 to 22 wt%, Fig. 1.2b and 2), and a considerable enrichment of the α-Fe phase (from 5% to 44% of α-Fe, Fig. 1.1c and 2). It should be pointed out that the complete conversion of Fe_3C into α-Fe is difficult to accomplish, since it requires temperatures at which the decomposition of the graphitic layers could occur.[78,79] Fig. 2 shows a graphical representation of the amount of Fe phases in our set of Fe@CNT derivatives.

Regarding the morphological characterization, low-resolution TEM investigations of **Fc-Fe@CNTs** (Fig. 3) allowed us to distinguish two categories of Fe@CNTs: those initially produced using ferrocene only during the CVD process (**Fc-Fe@CNTs**, **HCl-Fe@CNTs** and **Ann-Fe@CNTs**) are relatively short (modal classes of 0.4 to 0.6 μm in length and 5–10 nm in diameter according to the frequency histograms depicted in Fig. S2†) whereas those produced from a mixture of toluene and ferrocene (**Tol-Fe@CNTs**), are longer and wider (modal class of 1.4 to 1.6 μm in length and 25–30 nm in diameter). Importantly, no significant morphological differences have been observed and measured between the samples containing **Fc-Fe@CNTs**, **HCl-Fe@CNTs** and **Ann-Fe@CNTs**, suggesting that the main structural features of CNT nanostructures were preserved during the acidic washings and annealing treatments (Fig. 3a–c and S2†). On the other hand, the different size distribution of **Tol-Fe@CNTs** is probably due to a supplementary supply of carbon during their growth.

Regarding the Fe nanoparticles, those located at the tips of the CNTs are large spherical particles (between 20 and 70 nm) while conversely, the particles buried in the tubular cavities generally have the shape of nanorods (length up to 500 nm). This observation correlates well with the Fe encapsulation mechanism proposed by Kim *et al.* in which the iron layer in a growing carbon nanotube may be pinched off and forms discontinuous elongated iron particles inside the cavity.[80] Notably, core–shell Fe nanoparticles (Fe@CNPs) have also been observed, in which the graphitic layers wrap the spherical Fe phases in an onion-like fashion (Fig. 3a). Interestingly, the TEM images of **HCl-Fe@CNTs** (Fig. 3b and S3†) show a reduced content of the more spherical Fe@CNPs, while the elongated Fe rods confined in the CNTs seem unaltered, which is reflected in the frequency histograms of Fe particle size and aspect ratio distributions (Fig. S4†). These observations suggest that Fe@CNPs can be altered under acidic conditions, and thus easily removed with several washing cycles. Interestingly also, the Fe particles seemed to contract during annealing, taking smaller and more spherical shapes (the modal class of Fe particle dimensions passing from 30–40 nm in **HCl-Fe@CNTs** to 10–20 nm in **Ann-Fe@CNTs**, Fig. S4†). These observations are consistent with those of Kim *et al.* who remarked a similar "contraction" phenomenon occurring during the heating of their γ-rich Fe@CNTs at elevated temperatures (above 900 °C).[81]

High-resolution TEM (HR-TEM) studies were used to investigate the morphology and the phase of both exohedral and endohedral Fe-based nanostructures (Fig. 4). As already observed by LR-TEM, HR-TEM analyses further confirmed the presence of encapsulated Fe particles both as spherical and rod-like nanostructures surrounded by graphitic shells (*d*-spacing of 0.34 nm). The HR-TEM investigations carried out on several spheroidal/polygonal Fe nanostructures in **Fc-Fe@CNTs** and **HCl-Fe@CNTs** (Fig. 4a and b), shed further light on the crystallographic properties of the Fe nanostructures. In particular, as anticipated by the PXRD and ^{57}Fe-MS measurements (Fig. S1, 1.1a and b†), Fe_3C is the most abundant phase.

However, due to a subtle difference in the lattice spacing between the (011)-planes of α-Fe, (111)-planes of γ-Fe and (102)-, (220)-, (031)- and (112)-planes of Fe_3C (respectively of 2.03, 2.07, 2.07, 2.03, 2.01 and 1.97 Å), it is difficult to distinguish the γ-Fe, α-Fe and Fe_3C phases (Fig. 4a and Table S2†) when the three phases coexist. It is also noteworthy to mention that neither any particular crystal segregation between exohedral and endohedral Fe nanostructures nor preferential crystal plane alignments were observed in our samples, in contradiction with the observations of Kim *et al.* made on γ-Fe rich Fe@CNTs.[81]

The magnetic properties of the four Fe@CNT materials were assessed by recording hysteresis curves at 300 K, which allowed for the calculation of the magnetic saturation (M_s), coercivity (H_c) and low-field magnetic susceptibility (χ) values (Fig. 5 and S5, Tables 2 and S3†). In the case of the Fe_3C-enriched Fe@CNT derivatives, the M_s values decrease in the following order: **Fc-Fe@CNTs** > **Tol-Fe@CNTs** > **HCl-Fe@CNTs**. This clearly correlates to the Fe content. On the contrary, if one compares CNTs containing similar amounts of Fe, namely **HCl-Fe@CNTs** and **Ann-Fe@CNTs**, the M_s (higher for α-Fe)[33] and the coercivity (higher for Fe_3C)[82] of different ferromagnetic phases have also to be considered. In this respect,

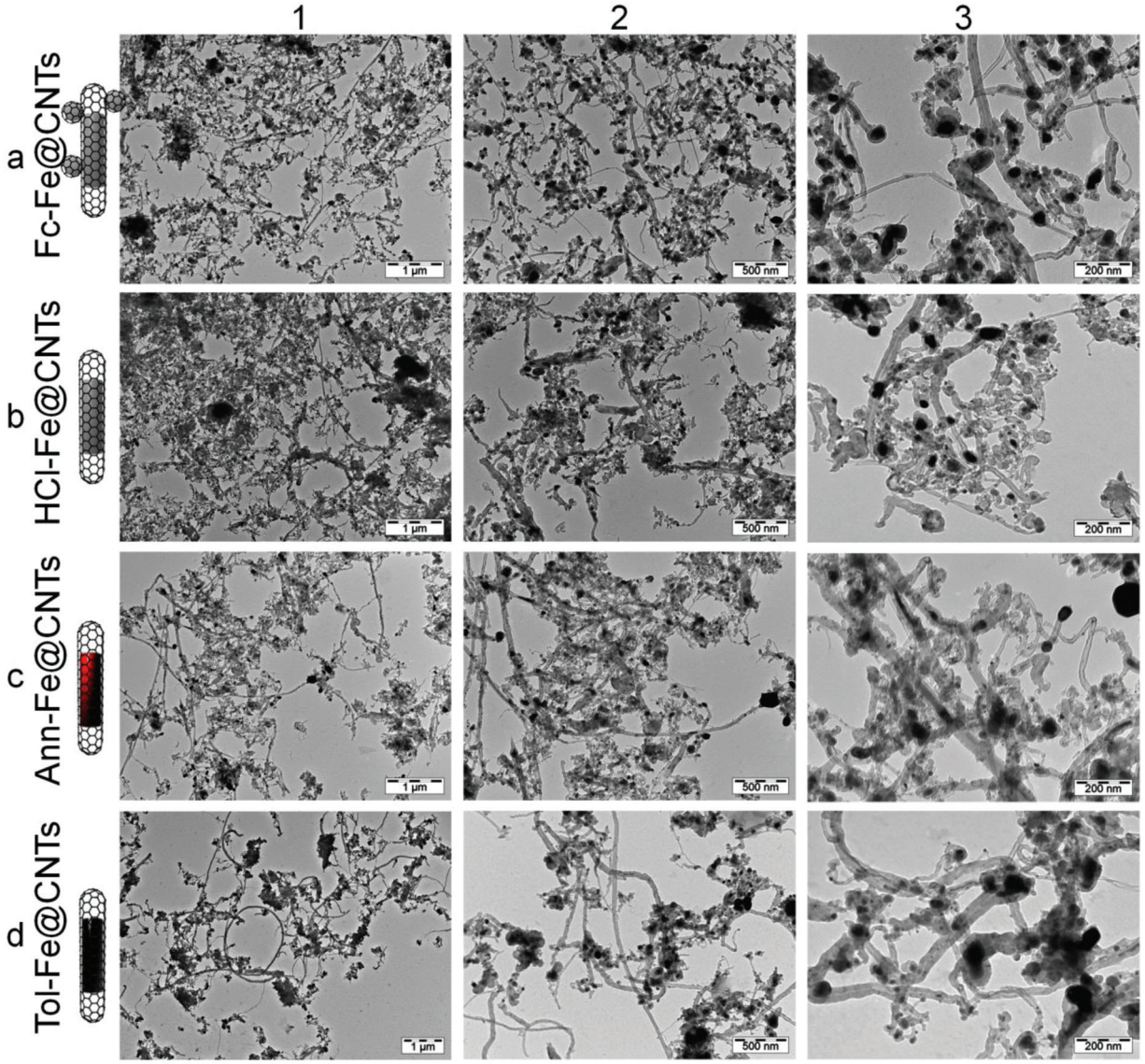

Fig. 3 Bright-field TEM images at different magnifications of the Fe@CNT derivatives as deposited from a suspension (0.1 mg mL^{-1}) onto Cu grids: (a) **Fc-Fe@CNTs**, (b) **HCl-Fe@CNTs**, (c) **Ann-Fe@CNTs** and (d) **Tol-Fe@CNTs**.

samples containing **Ann-Fe@CNTs** display the highest M_s (34 *vs.* 24 emu g^{-1}) and the smallest coercivity (430 *vs.* 570 Oe) as a consequence of the high α-Fe/Fe_3C ratio.[83] A moderate increase in the H_c value was also observed for the HCl-washed samples (from 550 to 570 Oe for **Fc-Fe@CNTs** and **HCl-Fe@CNTs**, respectively), caused by the significant loss of the exohedral Fe nanoparticles and the presence of the anisotropic, and thus highly coercive, endohedral Fe nanorods.[71]

2.2 Bioconjugation and physicochemical characterization

For the exohedral functionalization of the Fe@CNTs, we followed the covalent approach developed by Tour and co-workers.[84] We have selected the trimethylsilylethoxycarbonyl (**Teoc**) group for 4-aminobenzylamine **1** protection, as its removal does not require acidic treatments that could interfere with the Fe content and crystallinity. Teoc-protected aminobenzylamine **2** was thus prepared and reacted with the selected Fe@CNTs in the presence of isoamyl nitrite (Scheme 2), affording the functionalized material, **Fe@CNT–NHTeoc**.

The cleavage of the Teoc group using tetrabutylammonium fluoride (TBAF) afforded **Fe@CNT–NH_2** that, under typical amide ligation coupling conditions using EDC,[39,85] was transformed into **Fe@CNT–Ab** in the presence of the antibody. The intermediates were characterized by XPS, which revealed peaks at 101 and 400 eV for **Fe@CNT–NHTeoc**, attributed to the Si 2p and N 1s binding energies of the Teoc and amine groups, respectively (Fig. 6, columns 1 and 2, and S6–9†). TGA analysis under a N_2 atmosphere clearly shows a pyrolysis event in the range between 200 and 400 °C, suggesting a functionalization degree between 2 and 4 wt% for **Fe@CNT–NH_2** (Fig. 6, column 3,

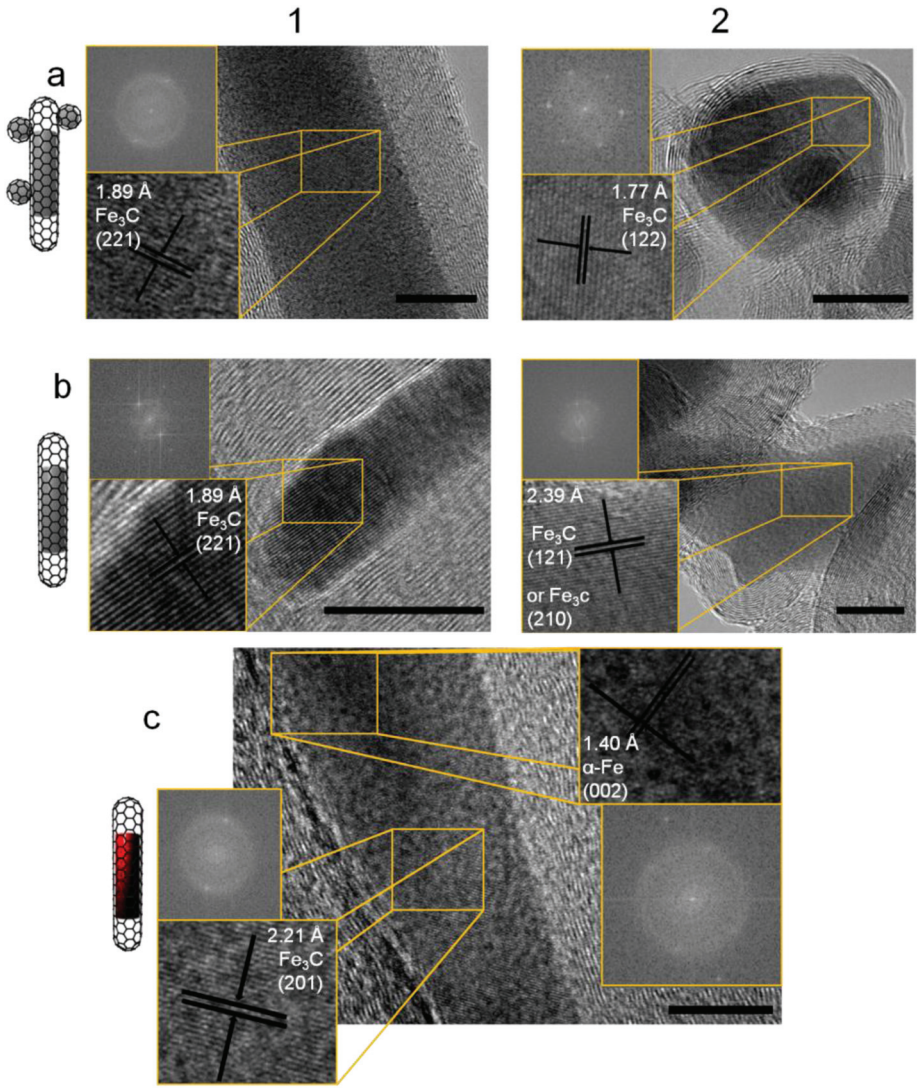

Fig. 4 HR-TEM images of the Fe nanostructures in (a) **Fc-Fe@CNTs**, (b) **HCl-Fe@CNTs** and (c) **Ann-Fe@CNTs**. FFT and direct distance measurements on some selected regions (orange rectangles) were used to estimate the inter-lattice distance value. For **Fc-Fe@CNTs** and **HCl-Fe@CNTs**, the typical Fe_3C cementite crystal lattice was observed, whereas for **Ann-Fe@CNTs** (c) α-Fe phases were also found. The corresponding lattice parameters are indexed directly on the image. Scale bar = 10 nm.

and S10†). Notably, TGA analysis under air shows similar Fe loading for the as-produced and the functionalized Fe@CNTs (Fig. S11†).

The XPS spectra of the samples after bioconjugation reveal a dramatic increase of both the oxygen (O 1s at 533 eV) and nitrogen atom content. The TGA plots of the bioconjugates show the typical protein signature at 350 °C (Fig. S10†) suggesting an average 20 wt% loading, and a Fe content of 30, 20, 16 and 15 wt% for **Fc-**, **Tol-**, **HCl-** and **Ann-Fe@CNT–Ab**, respectively (Table S5†).

2.3 *In vitro* magnetic performances

2.3.1 Magnetic cell filtration. The response of the Fe@CNT–Ab derivatives to a static magnetic field gradient is an important parameter if one wants to use them as a cell sorting device[86,87] and/or for filtration of biologically relevant species.[88,89] For this measurement, we have prepared water dispersions containing a given Fe@CNT–Ab derivative (at an equivalent Fe concentration of 30 μg mL^{-1}) and recorded the time-dependent UV-vis absorbance in the presence of a magnetic field gradient (Fig. 7a). The natural sedimentation of our materials was followed by the same method but in the absence of a magnet. Defining the "coagulation effectiveness" (**CE**) as the proportion of **Fe@CNT–Ab** removed from the water dispersion at a given time, one can calculate the **CE(*t*)** value following eqn (1):

$$\mathrm{CE}(t) = \left(1 - \frac{(\mathrm{Absorbance}(t) - \mathrm{Absorbance\ blank})}{(\mathrm{Absorbance}(t=0) - \mathrm{Absorbance\ blank})}\right) \times 100\,(\mathrm{in\ \%}) \quad (1)$$

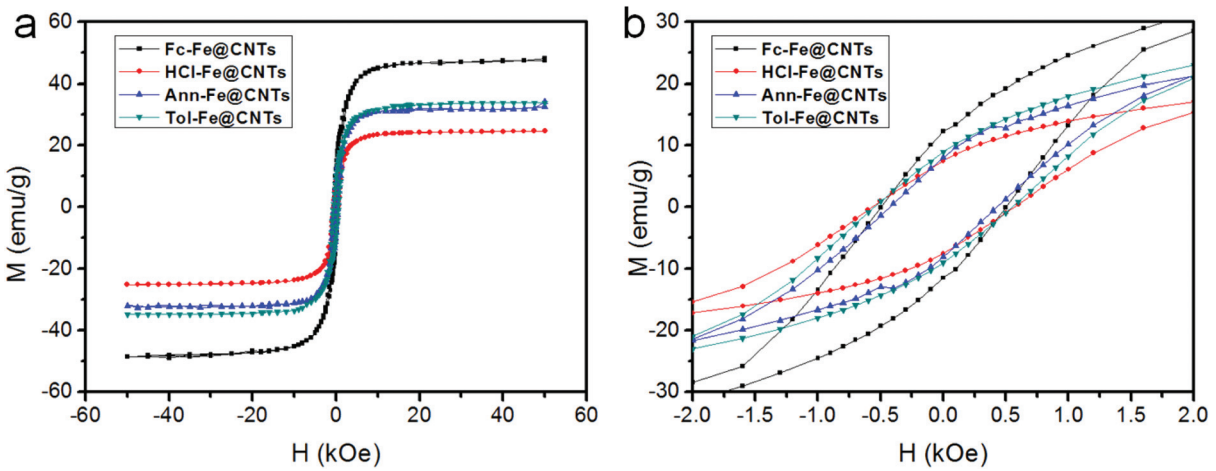

Fig. 5 Magnetization curves for the four Fe@CNTs substrates, (a) full traces (from −60 to +60 kOe) and (b) zoomed region (from −2 to +2 kOe).

Table 2 Magnetic parameters (M_s, H_c, χ and area of the hysteresis loop) for the four Fe@CNT hybrids

Hybrid	M_s (emu g^{-1})	M_s (emu g^{-1} Fe)	H_c (Oe)	χ (emu Oe^{-1} g^{-1})	$\oint M \times H$ (emu kOe g^{-1})	$\oint M \times H$ (emu kOe g^{-1} Fe)
Fc-Fe@CNTs	48	134	550	0.0216	63.18	176.5
HCl-Fe@CNTs	24	126	570	0.0118	36.05	189.7
Ann-Fe@CNTs	34	153	430	0.0174	24.08	108.9
Tol-Fe@CNTs	33	139	550	0.0165	45.14	189.7

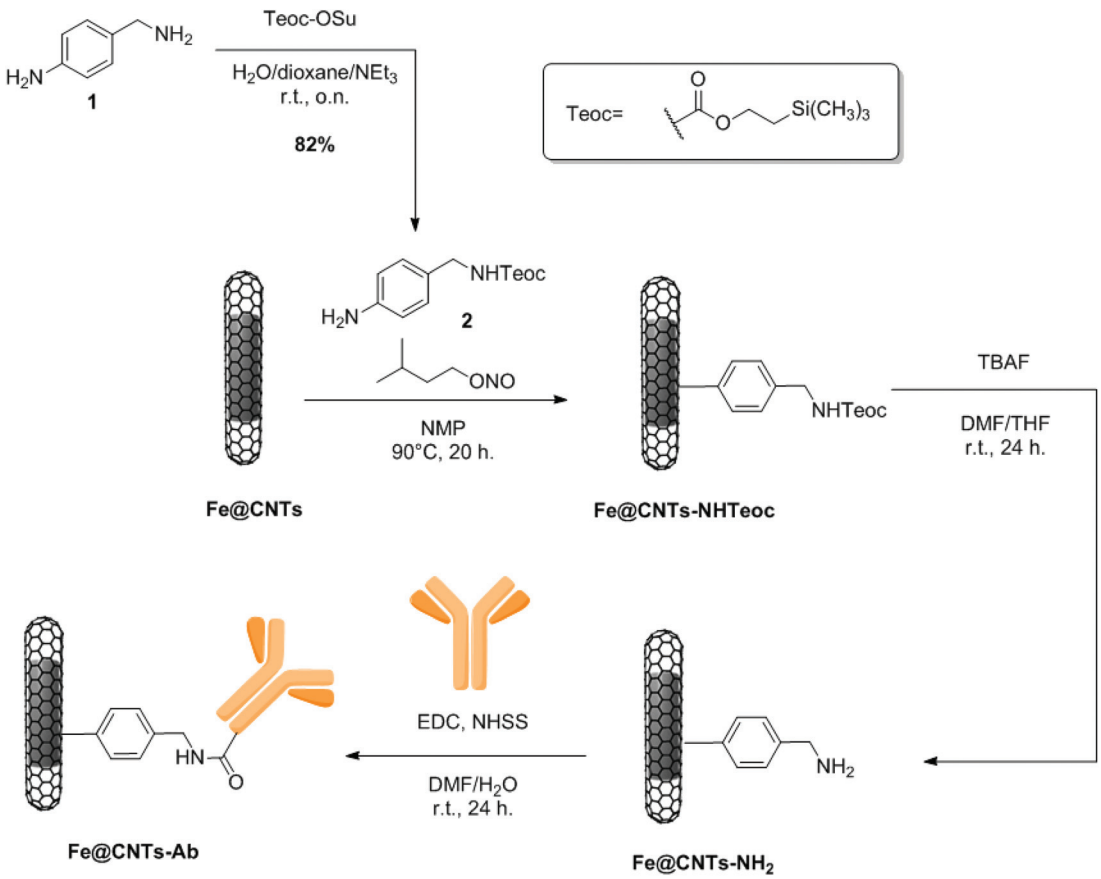

Scheme 2 Synthetic routes for the bioconjugation of Fe@CNTs.

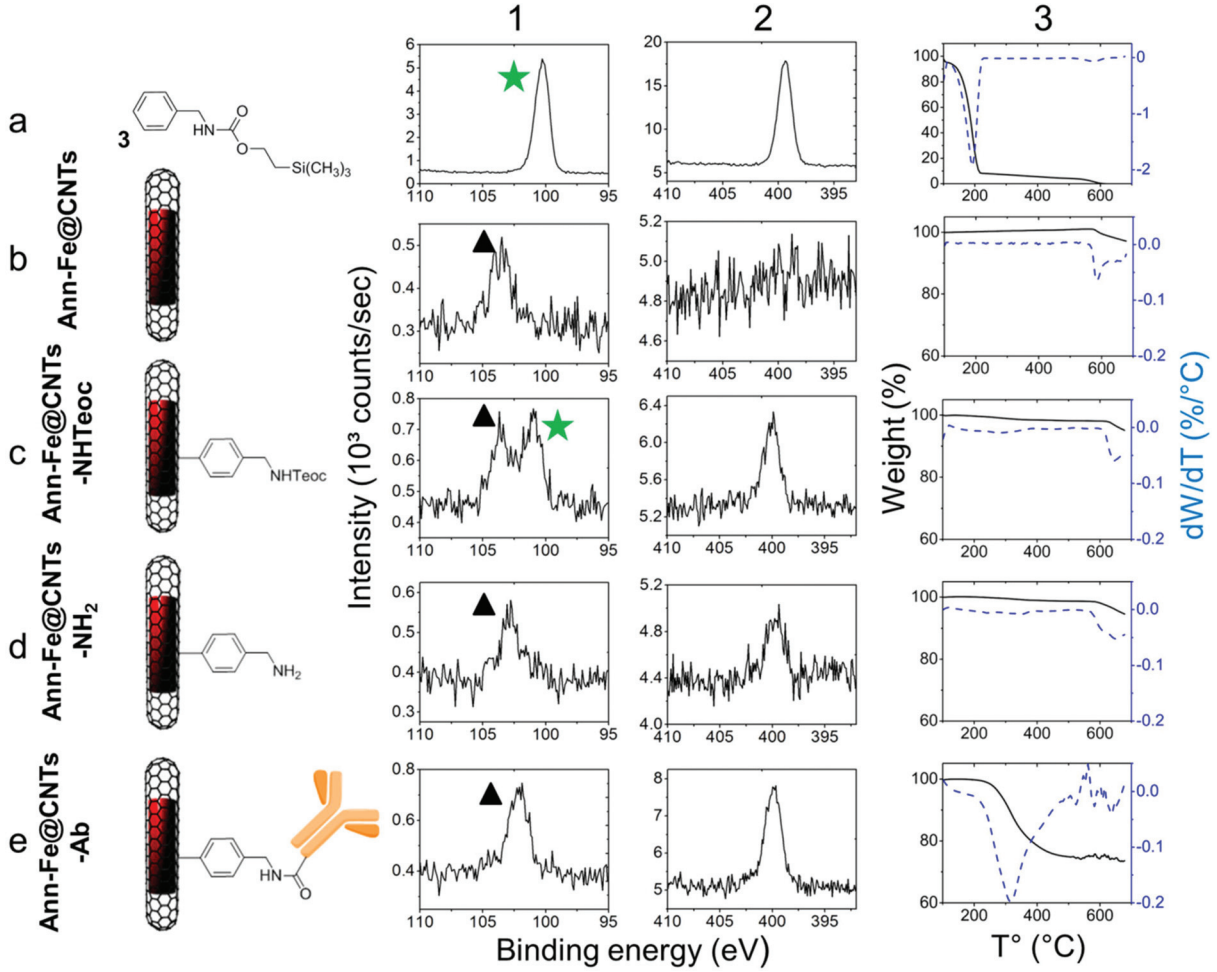

Fig. 6 High-resolution XPS spectra ((1) Si 2p and (2) N 1s) and (3) TGA under nitrogen profiles (temperature-modulated weight% (—) and differential weight% (------)) for reference (a) Teoc-benzylamine **3**, (b) **Ann-Fe@CNTs**, (c) **Ann-Fe@CNT–NHTeoc**, (d) **Ann-Fe@CNT–NH_2** and (e) **Ann-Fe@CNT–Ab**. The 101 eV peak (green star) fingerprints the Teoc protecting group, whereas the peak at 103 eV (black triangle) is attributed to a SiO_2 impurity.

The CE trend in the presence of a magnetic field suggests that the bioconjugates prepared from **Fc-Fe@CNTs** and **Tol-Fe@CNTs** behave similarly, whereas **HCl-Fe@CNT–Ab** and **Ann-Fe@CNT–Ab** are less effective as they display lower coagulation values. One can notice that this trend is very similar to that obtained in the absence of a magnetic field gradient, meaning that the dispersibility of our materials is the primary cause of their magnetic coagulation effectiveness. Their dispersibility most probably depends on the magnetic characteristics of the given Fe@CNTs, with those featuring the highest Fe loadings and the most coercive phase being the fastest to coagulate. In a subsequent experiment we have interfaced the four Fe@CNT–Ab bioconjugates with A431 cells, a model of epidermoid cancer cells over-expressing the epithelial growth factor receptors (EGFR) targeted by cetuximab.[39] Defining the "cell fishing effectiveness" (**CFE**) as the time-dependent population of cells remaining in a solution upon application of a given static magnetic field gradient (Fig. 7b and 8), one can also calculate the **CFE(t)** value defined as eqn (2):

$$\mathrm{CFE}(t) = \left(1 - \frac{\text{Cell density}(t)}{\text{Initial cell density}}\right) \times 100\,(\text{in }\%) \qquad (2)$$

From these measurements, it clearly appears that the best performing derivative is **HCl-Fe@CNT–Ab**, followed by **Tol-**, **Ann-** and finally **Fc-Fe@CNT–Ab**. This contrasts with the **CE** trend observed in the absence of the cells. Whereas the **CE** value reflects the properties of the material in the absence of the cells (it depends on the Fe loading and phase), the **CFE** analysis measures the efficiency to shepherd cells, thus embracing a complex system in which the bioconjugates are linked to a cell. This suggests that the Ab/Fe weight ratio also has to be accounted for the rationalisation of the data (Table S5†). As both the Fe concentration and the A431 cell density were constant, the **CFE** values clearly shows that the **HCl-Fe@CNT–Ab** and **Tol-Fe@CNT–Ab** bioconjugates

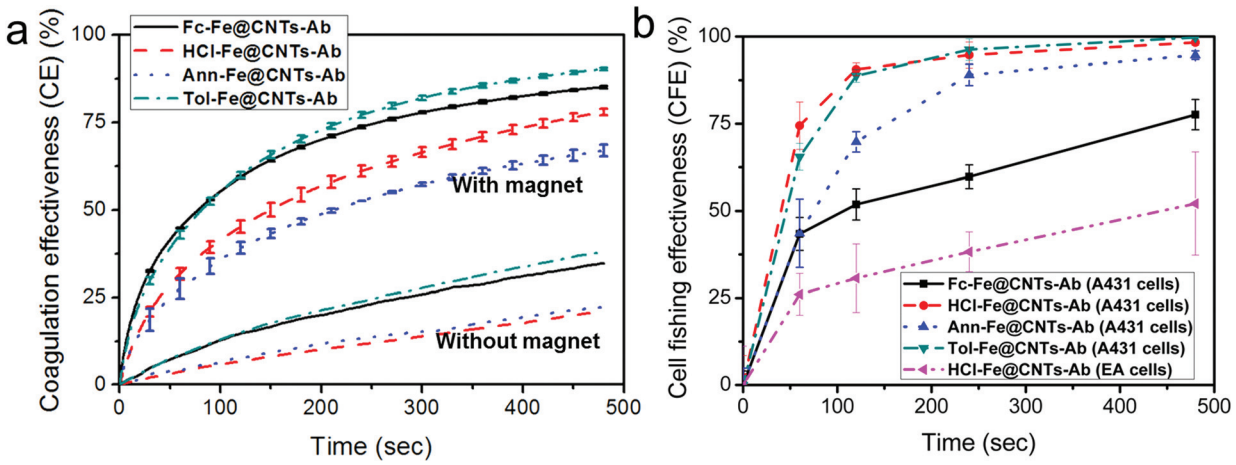

Fig. 7 (a) Time-dependent coagulation effectiveness for the Fe@CNT–Ab derivatives in the presence (upper curves) or in the absence (lower curves) of a magnet. The results are expressed as means ± 1 S.D. (n = 3, in the presence of a magnet and n = 1 in the absence of a magnet). (b) Magnetic cell filtration effectiveness of the **Fe@CNT–Ab** derivatives on A431 or EA cells. The results are expressed as means ± 1 S.D. (n = 3).

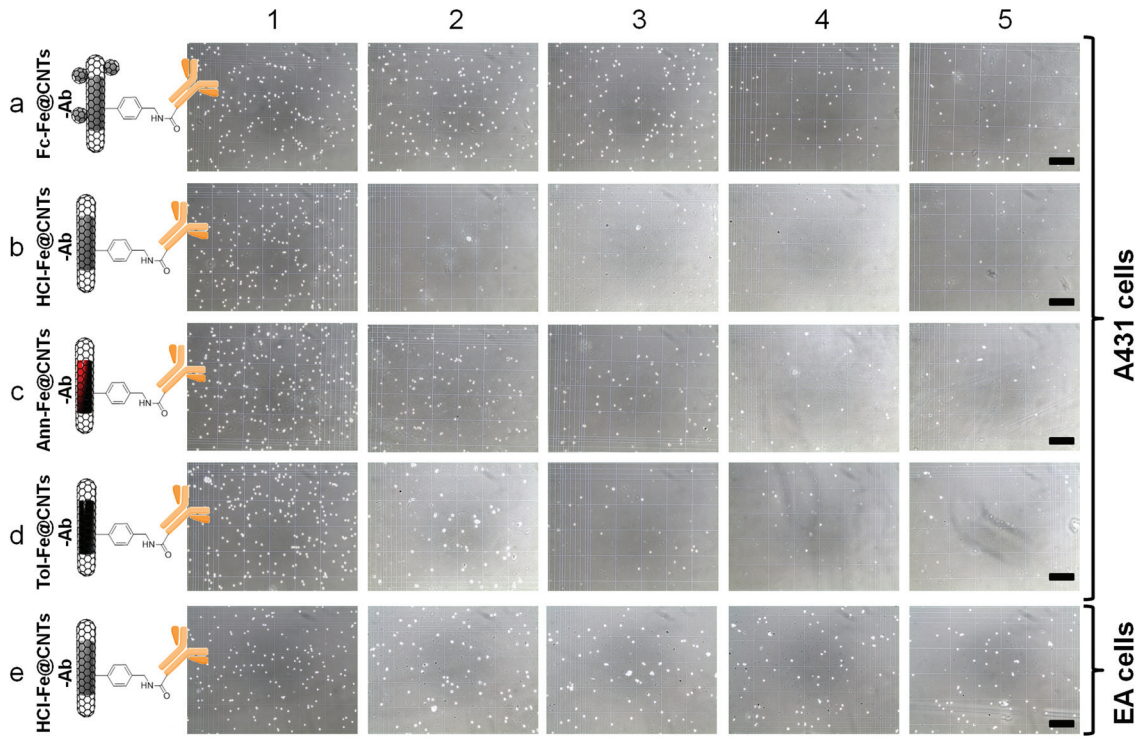

Fig. 8 Optical microscopy images displaying the cell content after (1) 0, (2) 60, (3) 120, (4) 240, (5) 480 seconds of magnetic fishing of A431 cells using (a) **Fc-Fe@CNT–Ab**, (b) **HCl-Fe@CNT–Ab**, (c) **Ann-Fe@CNT–Ab** or (d) **Tol-Fe@CNT–Ab** and fishing of EA cells with (e) **HCl-Fe@CNT–Ab**. Scale bar = 250 μm (all the images are at the same scale).

were the most effective materials, whereas **Fc-Fe@CNT–Ab** classified last and **Ann-Fe@CNT–Ab** displayed an intermediate behaviour. These data show that bioconjugates possessing high Ab/Fe ratios ensure a more efficient cellular binding, enhancing the shepherding action. Most likely, the difference between the **Ann-Fe@CNT–Ab** and **HCl-Fe@CNT–Ab** can be ascribed to the presence of phases displaying different coercivity values.

In parallel, the role of the antibody was assessed *via* a magnetic cell fishing using the best candidate **HCl-Fe@CNT–Ab** onto a control EGFR− cell line, *i.e.* EAhy926 (EA) cells. As expected, a remarkable reduction (25 *vs.* 75% after 1 min and

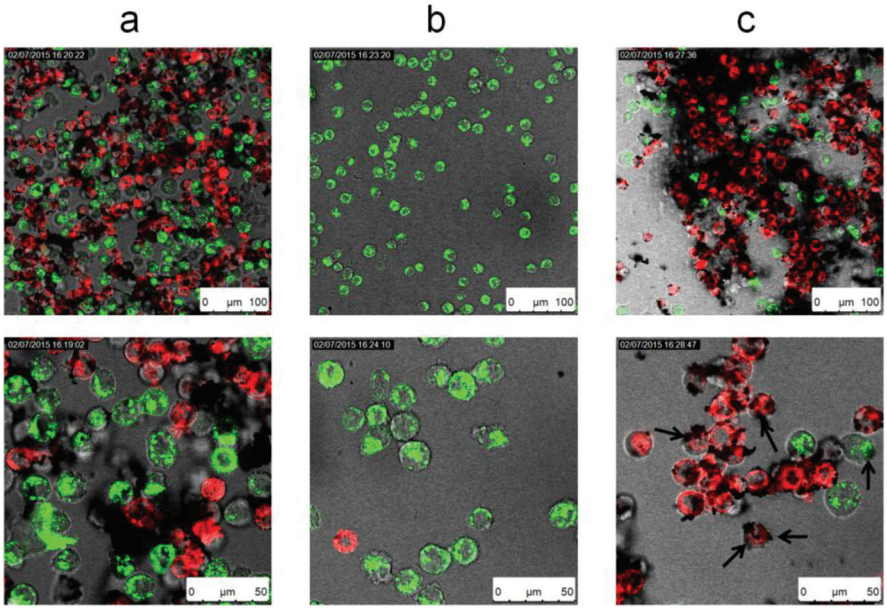

Fig. 9 Confocal microscopy images of (a) an initial mixture of **HCl-Fe@CNT–Ab**, A431 (red) and EA (green) cells and of (b) the supernatant and (c) the coagulate after 8 minutes of magnetic filtration. Black arrows indicate the presence of **HCl-Fe@CNT–Ab** aggregates, preferentially around A431 cells.

50 *vs.* 99% after 8 minutes, Fig. 7b and 8e) of the Cell Fishing Effectiveness (CFE) was observed, demonstrating the crucial role of the antibody as an anchoring unit toward EGFR+ cells. The intriguing relatively high percentage of EA cells nevertheless fished suggests the presence of a certain degree of aspecific binding. In order to know if this could hamper any selective removal of EGFR+ *vs.* EGFR− cells in a mixture of these two cell lines, EA and A431 cells were fluorescently stained in two different colours (red for A431 and green for EA), mixed together with HCl-Fe@CNT–Ab and placed against a magnet for 8 minutes (Fig. 9). The quasi-absence of A431 (red) cells remaining in the supernatant after this period of time along with a clear surrounding of A431 cells by CNTs in the precipitate indicate that selective binding occurs, allowing selective removal of the targeted EGFR+ cells over the non-targeted EGFR− cells. However, the presence of EA (green) cells in the magnetically-induced precipitate along with the observation of fewer black areas around some EA cells suggests the existence of a certain degree of non-specific binding of our CNTs towards these cells.

2.3.2 Magnetic fluid hyperthermia. Ferromagnetic particles exposed to an alternating magnetic field dissipate heat by hysteresis loss, and the dissipation efficiency of such heat is measured by the specific absorption rate (SAR) per mass of heating material, defined as eqn (3):[90,91]

$$\mathrm{SAR} = \frac{m_\mathrm{i}}{m_\mathrm{e}} \times \left(\frac{\mathrm{d}T}{\mathrm{d}t}\right) \times c_\mathrm{i}\,(\mathrm{W\,g^{-1}}) \qquad (3)$$

where c_i is the specific heat capacity of the fluid, m_i is the total mass of the fluid, m_e is the mass of the heating material and $\mathrm{d}T/\mathrm{d}t$ is the evolution of temperature of the ferrofluid as a function of time. The related heat generation can determine both the microscopic and bulk heating, and thus be exploited to affect cell viability by initiating cell death by apoptosis or necrosis.[27,92] We thus measured the SAR values of our set of **Fe@CNT–Ab** bioconjugates at a constant Fe concentration of 125 μg $\mathrm{mL^{-1}}$ in a complete cell medium (whose c_i was approximated to 4.185 J $\mathrm{g^{-1}\ K^{-1}}$), using alternating magnetic fields (220 kHz and amplitude in the range of 45–75 kA $\mathrm{m^{-1}}$) and recording the temperature evolution over time (Fig. S12†). Being under non-adiabatic conditions, $\mathrm{d}T/\mathrm{d}t$ values were obtained by performing a Box Lucas exponential fitting of the T *vs.* t curve and then calculating the slope $\mathrm{d}T/\mathrm{d}t$ at t_0 as reported in the literature.[93] The experimental SAR values of our CNT-based bioconjugates range from a minimum of 300 W $\mathrm{g^{-1}}$ at 45 kA $\mathrm{m^{-1}}$ to a maximum around 2000 W $\mathrm{g^{-1}}$ at 75 kA $\mathrm{m^{-1}}$, showing some pronounced differences depending on the Fe content and phase crystallinity (Fig. 10).

For ferromagnetic particles, SAR is mainly caused by hysteresis loss and it can be estimated from the following equation (eqn (4)):[43]

$$\mathrm{SAR} = \mu_0 \times f \times \oint M \times H \qquad (4)$$

with μ_0 being the vacuum magnetic permeability, f the frequency (Hz), and $\oint M \times H$ the area of the hysteresis loop (Fig. 5 and Table 2). The whole hysteresis area is obtained only when the magnetic field (H) is higher than the saturation field that, for our Fe@CNT derivatives, is around 20 kOe, corresponding to the amplitudes of about 1600 kA $\mathrm{m^{-1}}$. Since during the SAR measurements we used a dynamic field with amplitudes up to 75 kA $\mathrm{m^{-1}}$, it is very likely that we did not fully

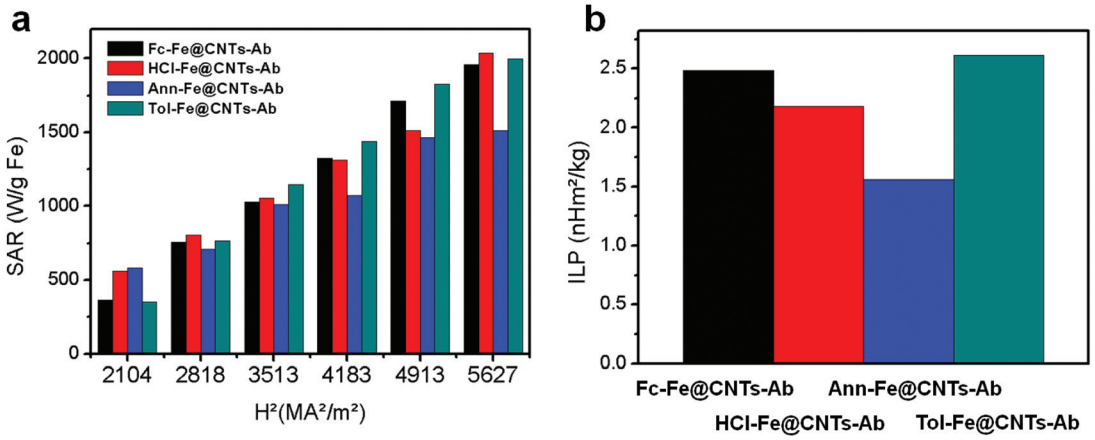

Fig. 10 (a) SAR at different magnetic field strengths and (b) ILP values for the four Fe@CNT–Ab.

Table 3 Theoretical (SAR_{th}) and experimental (SAR_{exp}) SAR values at 220 kHz and 75 kA m^{-1} for the four Fe@CNT hybrids

Hybrid	SAR_{th} (kW g^{-1} Fe)	SAR_{exp} (kW g^{-1} Fe)	SAR_{ex}/SAR_{th}
Fc-Fe@CNTs	3.88	1.96	0.50
HCl-Fe@CNTs	4.17	2.04	0.49
Ann-Fe@CNTs	2.40	1.51	0.63
Tol-Fe@CNTs	4.18	2.00	0.48

exploit the hysteresis loss. This suggests that the theoretical SAR values (SAR_{th}, calculated from eqn (4) using the SQUID analysis), are likely to be bigger than those obtained experimentally (SAR_{exp}, Table 3). Interestingly, the SAR_{exp}/SAR_{th} ratios of **Fc-**, **Tol-** and **HCl-Fe@CNT–Ab** are very similar, while **Ann-Fe@CNT–Ab** displayed a higher ratio. This discrimination well correlates with the lower coercivity and hysteresis area of **Ann-Fe@CNT–Ab** compared to those of the other bioconjugates. It should be pointed out that a similar trend of inverse proportionality between the coercivity and SAR values was already observed for ferromagnetic Fe_3O_4 nanoparticles by Ma *et al.*[94]

In order to compare the performances of our materials with commercially available Fe MNPs, we used a system-independent parameter introduced by Kallumadil *et al.*[93] called the Intrinsic Loss Power (ILP), defined as (eqn (5)):

$$\mathrm{ILP} = \frac{\mathrm{SAR}}{Hf} \qquad (5)$$

with H being the external magnetic field strength applied (A m^{-1}) and f the frequency (Hz). Compared to other Fe MNPs, the hyperthermia performances of our Fe@CNTs can be grouped in the upper range, since on 16 different commercial MNPs analysed by Kallumadil *et al.*[93] only four (100 and 130 nm Micromod's Nanomag-D-spio, Bayer's Resovist and Chemicell's FluidMAG-D) showed higher ILP values (respectively 3.12, 2.31, 3.1 and 2.67 nH m^2 kg^{-1}) than our best candidate **Tol-Fe@CNTs** (2.05 nH m^2 kg^{-1}).

In vitro magnetic fluid hyperthermia studies were then performed by suspending the EGFR+ overexpressing A431 cells and the chosen Fe@CNT–Ab at a constant Fe concentration of 125 μg mL^{-1}. To avoid bulk overheating, we thermostated the suspension and used pulsed magnetic fields (40 seconds per minute for 30 minutes, Fig. 11a). It is important to note that, to the best of our knowledge, the idea of using pulsed magnetic fields is quite recent. In particular, Rosania and coworkers recently demonstrated the advantage of this approach to improve the transport of iron oxide nanoparticles through cell barriers.[95] In our case, the pulses allow us to take an advantage of the high hyperthermic potential of our coercive Fe@CNTs at high fields (85 kA m^{-1}) without damaging non-targeted cells.

For each MFH test, the cell mortality was assessed by trypan blue staining and was accompanied by three negative controls (cells mixed or not mixed with Fe@CNT–Ab isothermally kept at 37 °C and cells exposed to the pulsed magnetic field conditions without Fe@CNTs) and one positive control (cells maintained at 70 °C). It emerged that **HCl-Fe@CNT–Ab** has significantly better hyperthermia activity (induction of around 70% mortality) than the other derivatives, which induced a cell death ranging from 15% to 40% (Fig. 11c). The comparison between **HCl-** and **Ann-Fe@CNT–Ab** is of particular interest since the two materials mainly differ in the Fe_3C/α-Fe ratio. As expected, the higher the proportion of the Fe_3C phase, the higher the SAR, and thus the hyperthermia efficiency. On the other hand, **Fc-** and **Tol-Fe@CNTs** are the least cytotoxic, probably due to the lower CNT concentration necessary to keep the same Fe concentration. This finding is of particular importance, as it suggests that a good balance between the Fe loading per nanotube and total concentration of CNTs is necessary if one wants to maximize the cytotoxic action of these hybrids.

Finally, the role of the antibody in the MFH-induced cytotoxic effect was performed using our best material, *i.e.* **HCl-Fe@CNT–Ab**, onto EA cells instead of A431 cells, all other parameters being kept identical (Fig. 11c, 12th and 13th bars).

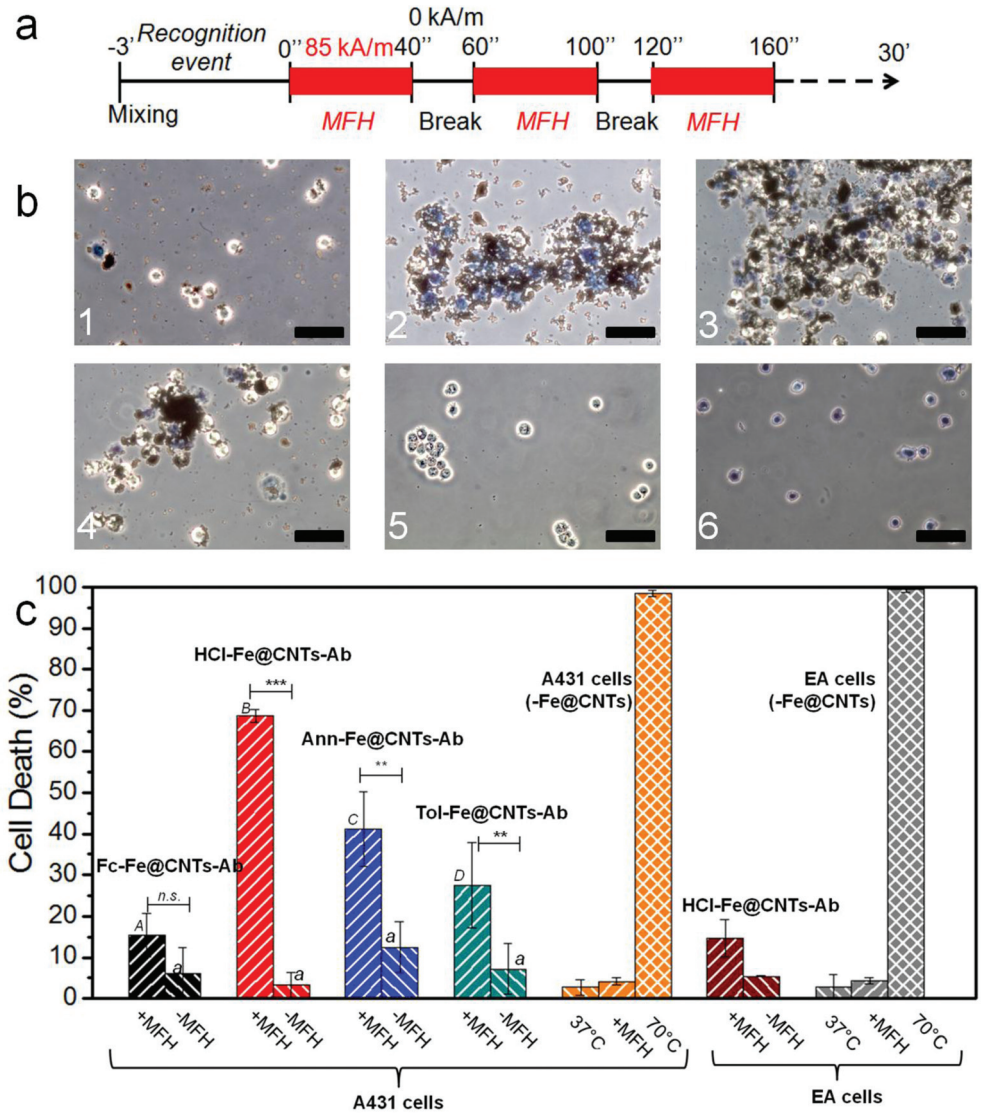

Fig. 11 (a) Timeline of the pulsed MFH conditions (40 s of impulse each minute for 30 minutes). (b) Phase contrast microscopy images of EGFR+ A431 cells after "pulsed" MFH incubation with **Fc-Fe@CNT–Ab** (1), **HCl-Fe@CNT–Ab** (2), **Ann-Fe@CNT–Ab**, (3) **Tol-Fe@CNT–Ab** (4) and with conventional heating at 37 °C (5) and at 70 °C (6). After the incubation, cells were stained with trypan blue. Scale bar = 50 μm. (c) Cell death as assayed with trypan blue staining; the results are expressed as means ± 1 S.D. (n = 3). ANOVA-2 (Holm–Šídák method): ***: $p < 0.001$, **: $p < 0.01$ and n.s.: $p > 0.05$. For comparisons for factors Fe@CNTs within "+MFH" and for Fe@CNTs within "–MFH", conditions with different letters (on top of the bar) have significantly different means ($p < 0.05$).

A severe reduction (15% for EA cells *vs.* 70% for A431 cells) in mortality rates was observed, confirming the crucial role of the antibody in the surrounding of the targeted cell membranes, leading to an efficient local heating effect and *in fine* cell death.

3. Conclusion

Using a combination of CVD and post-synthetic annealing protocols, we have successfully prepared a series of Fe@CNTs featuring diverse Fe phases and loadings in a controlled fashion. These materials undergo different responses under either static or dynamic magnetic fields depending on the magneto-crystalline characteristics of the inner metal phases. For instance, MFH experiments revealed that Fe@CNTs containing greater amounts of the more coercive Fe_3C phase display higher SAR values (~2 kW g^{-1} Fe) when compared to samples enriched in α-Fe (~1.5 kW g^{-1} Fe) at high fields (75 kA m^{-1}). Successive organic functionalization of the exohedral graphitic layer, followed by conjugation with a cancer-cell targeting antibody, yields bioactive Fe@CNT–Ab hybrids. It has been shown that these hybrids allow a rapid (after a few minutes) and very selective catching of a population of cancer cells over healthy

ones and are able to provoke their death (up to 70%) upon applications of pulsed MFH treatments. Specifically, it has been found that an ideal ratio of 1.2 Ab/Fe is necessary to efficiently interface with the cellular bodies facilitating their removal. In agreement with the SAR values, the hybrids containing higher percentages of Fe_3C for a given Fe/C ratio display higher cytotoxicity levels using our MFH protocol. Moreover, at an equivalent Fe concentration, higher cytotoxic effects were observed for the nanotubes exhibiting lower Fe/C ratios. These observations suggest that an optimal combination between the total amount of Fe, the type of Fe phase and the Ab loading is needed to prepare efficient Fe@CNTs for the magnetic-triggered biomedical applications. In particular, we think that a synergistic effect between the Ab loading and the Fe distribution in each kind of Fe@CNT exists, for which the maximum shepherding and hyperthermia effects are observed when higher densities of Fe@CNTs featuring the more coercive phase are interfaced with the cells.

Acknowledgements

This work was supported by the Belgian National Research Foundation (FRFC contract no. 2.4.550.09), the "TINTIN" ARC project from the Belgian French Community (Contract No. 09/14-023), the Wallonia Region (THERAPLUS project), the Science Policy Office of the Belgian Federal Government (BELSPO-IAP 7/05 project), the EU through the ERC Starting Grant "COLORLANDS" and the FP7 NMP small collaborative project "SACS" (Grant agreement no. 310651), the MIUR (FIRB Futuro in Ricerca SUPRACARBON, contract no. RBFR10DAK6). R.M. and F.P. thank the Fund for Scientific Research (FNRS) for their postdoctoral and FRIA doctoral fellowships, respectively. Y.G. thanks the cost action MP1202 for the funding. The authors also greatly thank Tanja Miletic for the TGA measurements, Bernadette Norberg for the help in the PXRD analyses and Corry Charlier for the acquisition of the TEM images ("Morphology-Imaging" technological platform of the UNamur). A.L.T and A.N.K. acknowledge the support of the Engineering and Physical Sciences Research Council (EPSRC) and the Nottingham Nanotechnology & Nanoscience Centre (NNNC).

References

1 M. Ferrari, *Nat. Rev. Cancer*, 2005, **5**, 161–171.
2 A. K. Iyer, G. Khaled, J. Fang and H. Maeda, *Drug Discovery Today*, 2006, **11**, 812–818.
3 Y. Matsumura and H. Maeda, *Cancer Res.*, 1986, **46**, 6387–6392.
4 S. Ganta, H. Devalapally, A. Shahiwala and M. Amiji, *J. Controlled Release*, 2008, **126**, 187–204.
5 A. M. A. Elhissi, W. Ahmed, I. U. Hassan, V. R. Dhanak and A. D'Emanuele, *J. Drug Delivery*, 2012, **2012**, 1–10.
6 C. Fabbro, H. Ali-Boucetta, T. Da Ros, K. Kostarelos, A. Bianco and M. Prato, *Chem. Commun.*, 2012, **48**, 3911–3926.
7 S. Y. Madani, N. Naderi, O. Dissanayake, A. Tan and A. M. Seifalian, *Int. J. Nanomed.*, 2011, **6**, 2963–2979.
8 S. K. Vashist, D. Zheng, G. Pastorin, K. Al-Rubeaan, J. H. T. Luong and F. S. Sheu, *Carbon*, 2011, **49**, 4077–4097.
9 A. Bianco, K. Kostarelos and M. Prato, *Curr. Opin. Chem. Biol.*, 2005, **9**, 674–679.
10 M. Prato, K. Kostarelos and A. Bianco, *Acc. Chem. Res.*, 2008, **41**, 60–68.
11 G. Lamanna, A. Garofalo, G. Popa, C. Wilhelm, S. Bégin-Colin, D. Felder-Flesch, A. Bianco, F. Gazeau and C. Ménard-Moyon, *Nanoscale*, 2013, **5**, 4412–4421.
12 K. Kostarelos, L. Lacerda, G. Pastorin, W. Wu, S. Wieckowski, J. Luangsivilay, S. Godefroy, D. Pantarotto, J. Briand, S. Muller, M. Prato and A. Bianco, *Nat. Nanotechnol.*, 2007, **2**, 108–113.
13 N. W. S. Kam, Z. Liu and H. Dai, *Angew. Chem., Int. Ed.*, 2006, **45**, 577–581.
14 K. Kostarelos, A. Bianco and M. Prato, *Nat. Nanotechnol.*, 2009, **4**, 627–633.
15 Z. Liu, S. Tabakman, K. Welsher and H. Dai, *Nano Res.*, 2009, **2**, 85–120.
16 R. Singh and S. V. Torti, *Adv. Drug Delivery Rev.*, 2013, **65**, 2045–2060.
17 A. N. Khlobystov, *ACS Nano*, 2011, **5**, 9306–9312.
18 D. A. Britz and A. N. Khlobystov, *Chem. Soc. Rev.*, 2006, **35**, 637–659.
19 A. N. Khlobystov, D. A. Britz and G. A. D. Briggs, *Acc. Chem. Res.*, 2005, **38**, 901–909.
20 R. Marega and D. Bonifazi, *New J. Chem.*, 2014, **38**, 22–27.
21 S. Y. Hong, G. Tobias, K. T. Al-Jamal, B. Ballesteros, H. Ali-Boucetta, S. Lozano-Perez, P. D. Nellist, R. B. Sim, C. Finucane, S. J. Mather, M. L. H. Green, K. Kostarelos and B. G. Davis, *Nat. Mater.*, 2010, **9**, 485–490.
22 P. Caravan, J. J. Ellison, T. J. McMurry and R. B. Lauffer, *Chem. Rev.*, 1999, **99**, 2293–2352.
23 R. D. Bolskar, A. F. Benedetto, L. O. Husebo, R. E. Price, E. F. Jackson, S. Wallace, L. J. Wilson and J. M. Alford, *J. Am. Chem. Soc.*, 2003, **125**, 5471–5478.
24 B. Sitharaman, K. R. Kissell, K. B. Hartman, L. A. Tran, A. Baikalov, I. Rusakova, Y. Sun, H. A. Khant, S. J. Ludtke, W. Chiu, S. Laus, E. Tóth, L. Helm, A. E. Merbach and L. J. Wilson, *Chem. Commun.*, 2005, 3915–3917.
25 Z. Gu, H. Peng, R. H. Hauge, R. E. Smalley and J. L. Margrave, *Nano Lett.*, 2002, **2**, 1009–1013.
26 R. Qiao, C. Yang and M. Gao, *J. Mater. Chem.*, 2009, **19**, 6274–6293.
27 S. Laurent, S. Dutz, U. O. Häfeli and M. Mahmoudi, *Adv. Colloid Interface Sci.*, 2011, **166**, 8–23.
28 C. Plank, F. Scherer, U. Schillinger, M. Anton and C. Bergemann, *Gene Ther.*, 2002, **9**, 102–109.
29 X. Liu, I. Marangon, G. Melinte, C. Wilhelm, C. Ménard-Moyon, B. P. Pichon, O. Ersen, K. Aubertin, W. Baaziz,

C. Pham-Huu, S. Bégin-Colin, A. Bianco, F. Gazeau and D. Bégin, *ACS Nano*, 2014, **8**, 11290–11304.
30 P. Kappen, A. Rider, P. J. Pigram and N. Brack, *J. Phys. Chem. C*, 2011, **115**, 21083–21087.
31 J. P. Tessonnier, G. Winé, C. Estournès, C. Leuvrey, M. J. Ledoux and C. Pham-Huu, *Catal. Today*, 2005, **102–103**, 29–33.
32 W. Chen, X. Pan and X. Bao, *J. Am. Chem. Soc.*, 2007, **129**, 7421–7426.
33 H. M. Lu, W. T. Zheng and Q. Jiang, *J. Phys. D: Appl. Phys.*, 2007, **40**, 320–325.
34 D. Cai, J. M. Mataraza, Z.-H. Qin, Z. Huang, J. Huang, T. C. Chiles, D. Carnahan, K. Kempa and Z. Ren, *Nat. Methods*, 2005, **2**, 449–454.
35 V. Raffa, O. Vittorio, G. Ciofani, V. Pensabene and A. Cuschieri, *Nanoscale Res. Lett.*, 2010, **5**, 257–262.
36 V. Pensabene, O. Vittorio, V. Raffa, A. Ziaei, A. Menciassi and P. Dario, *IEEE Trans. Nanobiosci.*, 2008, **7**, 105–110.
37 O. Vittorio, P. Quaranta, V. Raffa, N. Funel, D. Campani, S. Pelliccioni, B. Longoni, F. Mosca, A. Pietrabissa and A. Cuschieri, *Nanomedicine*, 2011, **6**, 43–54.
38 X. Ding, R. Singh, A. Burke, H. Hatcher, J. Olson, R. A. Kraft, M. Schmid, D. Carroll, J. D. Bourland, S. Akman, F. M. Torti and S. V. Torti, *Nanomedicine*, 2011, **6**, 1341–1352.
39 R. Marega, F. De Leo, F. Pineux, J. Sgrignani, A. Magistrato, A. D. Naik, Y. Garcia, L. Flamant, C. Michiels and D. Bonifazi, *Adv. Funct. Mater.*, 2013, **23**, 3173–3184.
40 M. Kumar and Y. Ando, *J. Nanosci. Nanotechnol.*, 2010, **10**, 3739–3758.
41 U. Weissker, S. Hampel, A. Leonhardt and B. Büchner, *Materials*, 2010, **3**, 4387–4427.
42 J. Graham, M. Muhsin and P. Kirkpatrick, *Nat. Rev. Drug Discovery*, 2004, **3**, 549–550.
43 Y. Krupskaya, C. Mahn, A. Parameswaran, A. Taylor, K. Krämer, S. Hampel, A. Leonhardt, M. Ritschel, B. Büchner and R. Klingeler, *J. Magn. Magn. Mater.*, 2009, **321**, 4067–4071.
44 A. V. Ellis and B. Ingham, *J. Magn. Magn. Mater.*, 2006, **302**, 378–381.
45 I. W. Chiang, B. E. Brinson, R. E. Smalley, J. L. Margrave and R. H. Hauge, *J. Phys. Chem. B*, 2001, **105**, 1157–1161.
46 S. Groudeva-Zotova, R. Kozhuharova, D. Elefant, T. Mühl, C. M. Schneider and I. Mönch, *J. Magn. Magn. Mater.*, 2006, **306**, 40–50.
47 X. Gui, J. Wei, K. Wang, W. Wang, R. Lv, J. Chang, F. Kang, J. Gu and D. Wu, *Mater. Res. Bull.*, 2008, **43**, 3441–3446.
48 A. G. Osorio, L. G. Pereira, J. B. M. Da Cunha and C. P. Bergmann, *Mater. Res. Bull.*, 2013, **48**, 4168–4173.
49 C. N. R. Rao and R. Sen, *Chem. Commun.*, 1998, 1525–1526.
50 R. Sen, A. Govindaraj and C. N. R. Rao, *Chem. Phys. Lett.*, 1997, **267**, 276–280.
51 S. B. Sinnott, R. Andrews, D. Qian, A. M. Rao, Z. Mao, E. C. Dickey and F. Derbyshire, *Chem. Phys. Lett.*, 1999, **315**, 25–30.
52 K. Kuwana and K. Saito, *Carbon*, 2005, **43**, 2088–2095.
53 Q. Liu, Z.-G. Chen, B. Liu, W. Ren, F. Li, H. Cong and H.-M. Cheng, *Carbon*, 2008, **46**, 1892–1902.
54 C. Müller, A. Leonhardt, M. C. Kutz, B. Büchner and H. Reuther, *J. Phys. Chem. C*, 2009, **113**, 2736–2740.
55 E. F. Antunes, V. G. de Resende, U. A. Mengui, J. B. M. Cunha, E. J. Corat and M. Massi, *Appl. Surf. Sci.*, 2011, **257**, 8038–8043.
56 J. Cheng, X. P. Zou, G. Zhu, M. F. Wang, Y. Su, G. Q. Yang and X. M. Lü, *Solid State Commun.*, 2009, **149**, 1619–1622.
57 A. G. Osorio and C. P. Bergmann, *Appl. Surf. Sci.*, 2013, **264**, 794–800.
58 A. Moisala, A. G. Nasibulin, D. P. Brown, H. Jiang, L. Khriachtchev and E. I. Kauppinen, *Chem. Eng. Sci.*, 2006, **61**, 4393–4402.
59 M. C. Schnitzler, M. M. Oliveira, D. Ugarte and A. J. G. Zarbin, *Chem. Phys. Lett.*, 2003, **381**, 541–548.
60 E. Muñoz-Sandoval, F. López-Urías, A. Díaz-Ortiz, M. Terrones, M. Reyes-Reyes and J. L. Morán-López, *J. Magn. Magn. Mater.*, 2004, **272–276**, E1255–E1257.
61 S. Costa, E. Borowiak-Palen, A. Bachmatiuk, M. H. Rümmeli, T. Gemming and R. J. Kalenczuk, *Energy Convers. Manage.*, 2008, **49**, 2483–2486.
62 R. Kozhuharova, M. Ritschel, D. Elefant, A. Graff, A. Leonhardt, I. Mönch, T. Mühl and C. M. Schneider, *J. Mater. Sci.: Mater. Electron.*, 2003, **14**, 789–791.
63 S. Hampel, A. Leonhardt, D. Selbmann, K. Biedermann, D. Elefant, C. Müller, T. Gemming and B. Büchner, *Carbon*, 2006, **44**, 2316–2322.
64 M. S. Shamsudin, N. A. Asli, S. Abdullah, S. Y. S. Yahya and M. Rusop, *Adv. Condens. Matter Phys.*, 2012, **2012**, 1–7.
65 H. Sato, A. Nagata, N. Kubonaka and Y. Fujiwara, *Jpn. J. Appl. Phys.*, 2013, **52**, 11NL03.
66 D. He, H. Li, W. Li, P. Haghi-Ashtiani, P. Lejay and J. Bai, *Carbon*, 2011, **49**, 2273–2286.
67 A. Leonhardt, S. Hampel, C. Müller, I. Mönch, R. Koseva, M. Ritschel, D. Elefant, K. Biedermann and B. Büchner, *Chem. Vap. Deposition*, 2006, **12**, 380–387.
68 W. Wang, K. Wang, R. Lv, J. Wei, X. Zhang, F. Kang, J. Chang, Q. Shu, Y. Wang and D. Wu, *Carbon*, 2007, **45**, 1127–1129.
69 X. Gui, K. Wang, W. Wang, J. Wei, X. Zhang, R. Lv, Y. Jia, Q. Shu, F. Kang and D. Wu, *Mater. Chem. Phys.*, 2009, **113**, 634–637.
70 V. Gupta and R. K. Kotnala, *Angew. Chem., Int. Ed.*, 2012, **51**, 2916–2919.
71 C. X. Shi and H. T. Cong, *J. Appl. Phys.*, 2008, **104**, 034307.
72 C. Müller, A. Leonhardt, S. Hampel and B. Büchner, *Phys. Status Solidi B*, 2006, **243**, 3091–3094.
73 A. Leonhardt, M. Ritschel and R. Kozhuharova, *Diamond Relat. Mater.*, 2003, **12**, 790–793.
74 M. Mayne, N. Grobert, M. Terrones, R. Kamalakaran, M. Rühle, H. W. Kroto and D. R. M. Walton, *Chem. Phys. Lett.*, 2001, **338**, 101–107.
75 C. Wang, R. Lv, F. Kang, J. Gu, X. Gui and D. Wu, *J. Magn. Magn. Mater.*, 2009, **321**, 1924–1927.

76 F. C. Dillon, A. Bajpai, A. Koós, S. Downes, Z. Aslam and N. Grobert, *Carbon*, 2012, **50**, 3674–3681.
77 C. T. Wirth, B. C. Bayer, A. D. Gamalski, S. Esconjauregui, R. S. Weatherup, C. Ducati, C. Baehtz, J. Robertson and S. Hofmann, *Chem. Mater.*, 2012, **24**, 4633–4640.
78 F. S. Boi, G. Mountjoy, R. M. Wilson, Z. Luklinska, L. J. Sawiak and M. Baxendale, *Carbon*, 2013, **64**, 351–358.
79 A. Leonhardt, M. Ritschel, D. Elefant, N. Mattern, K. Biedermann, S. Hampel, C. Müller, T. Gemming and B. Büchner, *J. Appl. Phys.*, 2005, **98**, 074315.
80 H. Kim and W. Sigmund, *Carbon*, 2005, **43**, 1743–1748.
81 H. Kim and W. Sigmund, *J. Cryst. Growth*, 2005, **276**, 594–605.
82 G. Zhang and S. Yu, *J. Phys.: Condens. Matter*, 1997, **9**, 1851–1855.
83 A. I. Ul'yanov, E. P. Elsukov, A. A. Chulkina, A. V. Zagainov, N. B. Arsent'eva, G. N. Konygin, V. F. Novikov and V. V. Isakov, *Russ. J. Non-destr. Test.*, 2006, **42**, 452–459.
84 J. L. Bahr and J. M. Tour, *Chem. Mater.*, 2001, **13**, 3823–3824.
85 R. Marega, L. Karmani, L. Flamant, P. G. Nageswaran, V. Valembois, B. Masereel, O. Feron, T. Vander Borght, S. Lucas, C. Michiels, B. Gallez and D. Bonifazi, *J. Mater. Chem.*, 2012, **22**, 21305–21312.
86 M. Arruebo, R. Fernández-Pacheco, M. R. Ibarra and J. Santamaría, *Nano Today*, 2007, **2**, 22–32.
87 V. I. Shubayev, T. R. Pisanic and S. Jin, *Adv. Drug Delivery Rev.*, 2009, **61**, 467–477.
88 H. Gu, K. Xu, C. Xu and B. Xu, *Chem. Commun.*, 2006, 941–949.
89 S. Bucak, D. A. Jones, P. E. Laibinis and T. A. Hatton, *Biotechnol. Prog.*, 2003, **19**, 477–484.
90 L. Lartigue, C. Innocenti, T. Kalaivani, A. Awwad, M. del M. Sanchez Duque, Y. Guari, J. Larionova, C. Gueírin, J. L. G. Montero, V. Barragan-Montero, P. Arosio, A. Lascialfari, D. Gatteschi and C. Sangregorio, *J. Am. Chem. Soc.*, 2011, **133**, 10459–10472.
91 M. Gonzales-Weimuller, M. Zeisberger and K. M. Krishnan, *J. Magn. Magn. Mater.*, 2009, **321**, 1947–1950.
92 C. S. S. R. Kumar and F. Mohammad, *Adv. Drug Delivery Rev.*, 2011, **63**, 789–808.
93 M. Kallumadil, M. Tada, T. Nakagawa, M. Abe, P. Southern and Q. A. Pankhurst, *J. Magn. Magn. Mater.*, 2009, **321**, 1509–1513.
94 M. Ma, Y. Wu, J. Zhou, Y. Sun, Y. Zhang and N. Gu, *J. Magn. Magn. Mater.*, 2004, **268**, 33–39.
95 K. A. Min, M. C. Shin, F. Yu, M. Yang, A. E. David, V. C. Yang and G. R. Rosania, *ACS Nano*, 2013, **7**, 2161–2171.